Received: 2July 2020 | Revised: 23 December 2020 | Accepted: 23 December 2020

DOI: 10.1002/kin.21474

INTERNATIONAL JOURNAL OF CHEMICAL KINETICS WILEY

AR TICLE

Kinetic studies of excited singlet oxygen atom O(^{1}D) reactions with ethanol

Hongtao Zhong[1] | **Chao Yan**[1] | **Chu C. Teng**[2] | **Timothy Y. Chen**[1] | **Gerard Wysocki**[2] | **Yiguang Ju**[1]

[1] Department of Mechanical and Aerospace Engineering, Princeton University, Princeton, NJ, USA

[2] Department of Electrical Engineering, Princeton University, Princeton, NJ, USA

Correspondence
Chao Yan, Department of Mechanical and Aerospace Engineering, Princeton University, Princeton, NJ 08544, USA.
Email: chaoy@princeton.edu

Funding information
U.S. Department of Energy, Plasma Science Center, Grant/Award Number: DE-SC0020233; U.S. Department of Energy, BES, Grant/Award Number: DE-SC0021135; Exxon Mobil Research Grant; DOE-NETL, Grant/Award Number: DE-FE0026825; National Science Foundation (NSF), Division of Chemical, Bioengineering, Environmental, and Transport Systems, Grant/Award Number: 1903362

Abstract

The multichannel reaction of excited singlet oxygen atom with ethanol, O(^{1}D) + C_2H_5OH (1), was studied in a photolysis flow reactor coupled with mid-infrared Faraday rotation spectroscopy (FRS) and UV-IR direct absorption spectroscopy (DAS) at 297 K with reactor pressures of 60, 120, and 150 Torr (bath He). The excited singlet oxygen atom was generated through the photolysis of O_3 at 266 nm. The photon flux and O(^{1}D) concentrations were determined by in situ actinometry based on O_3 depletion. Temporal profiles of OH and H_2O were monitored via DAS signals at ca. 3568.62 and 3568.29 cm^{-1}, while temporal profiles of HO_2 were measured via FRS signals at ca. 1396.90 cm^{-1}. The branching ratios of the target reaction (1) were determined by fitting temporal profiles to simulations from an in-house reaction mechanism. Two major reaction channels were identified as $CH_3CHOH + OH$ and $CH_3O + CH_2OH$, and their branching ratios were determined as 0.46 ± 0.12 and 0.42 ± 0.11, respectively. A specific HO_2 + RO_2 reaction between HO_2 and $O_2CH_2CH_2OH$ (β-RO_2) at the low-temperature range is estimated in this work as $HO_2 + O_2CH_2CH_2OH \longrightarrow$ products with a rate constant of 7×10^{-12} cm^3 $molecule^{-1}$ s^{-1}.

KEYWORDS
atmospheric kinetics, balanced detection, Faraday rotation spectroscopy, photolysis Herriott cell, plasma-assisted combustion, singlet oxygen atom

1 | INTRODUCTION

The electronically excited singlet oxygen atom O(^{1}D) is one of the most reactive species produced in nonequilibrium plasma.[1–3] O(^{1}D) attracts great interests from the physical chemistry society throughout the past few decades as it has a significant impact on atmospheric chemistry,[4,5] plasma-assisted material synthesis,[6–8] and plasma-assisted combustion.[2,3] Specifically, O(^{1}D) plays an active role in driving the chain branching of plasma-assisted low-temperature fuel oxidation and generating important low-temperature intermediate species including the hydroxyl radical (OH) and the hydroperoxyl radical (HO_2), leading to plasma-assisted cool flames.[9] Moreover, in atmospheric chemistry, with the development of shale gases[10,11] and biofuels,[12,13] the unburned leaked fuels may react with atmospheric species including O(^{1}D). The subsequent atmospheric chemical kinetics may greatly influence the O_3 cycle, smog formation, and climate change.[14,15] As such, understanding reactions of O(^{1}D) with fuels and following reactions involving HO_2 and OH would provide key insight into plasma-assisted fuel oxidation and fuel leakage effect on the atmospheric chemistry.

TABLE 1 Summary of reported rate constant values for reaction $O(^1D) + CH_3OH$ at room temperature

Products	k ($\times 10^{-10}$ cm^3 molecule^{-1} s^{-1})	Method	P (Torr)	Reference
$CH_3O + OH$	4.2 ± 0.1	VUV-LIF	1–2	[23]
$HOCH_2O + H$	0.9 ± 0.1	VUV-LIF	1–2	[23]
trans-$HOCH_2OH$	4.2	PES calculation	0.1	[24]
CH_3OOH	0.5	PES calculation	0.1	[24]

Abbreviations: PES, potential-energy surface; VUV-LIF, vacuum-UV laser-induced fluorescence.

Unfortunately, $O(^1D)$ reactions with fuels are complicated by the insertion/decomposition mechanism and multichannel dynamics. Most previous studies of $O(^1D)$ reactions with fuels are focused on small saturated hydrocarbons,[16–20] where the excited oxygen atom could insert into C–H or C–C bond for hydrocarbons (RH) to form an energetic complex[19] and eventually undergo fragmentation and produce radicals with different low-temperature reactivities. $O(^1D)$ reactions with oxygenated fuels including alcohols are less examined,[21–26] where $O(^1D)$ could possibly insert into C–O or O–H bond, leading to more complex kinetics. The earliest experimental attempt of $O(^1D)$ reactions with alcohols was made by Osif et al.[21] By photolyzing $N_2O/CH_3OH/CO$ at 213 nm (298 K, 345 K, and the milliTorr pressure range) and analyzing the product with the gas chromatograph, they concluded that the OH production channel had a branching ratio of 0.46 ± 0.10 while the deactivation channel $CH_3OH + O(^1D) \longrightarrow CH_3OH + O(^3P)$ is negligible (≤0.05). No measurements of absolute rate constants for $CH_3OH + O(^1D)$ were provided. Later in 1983, Goldstein and Wiesenfeld[22] applied laser-induced fluorescence (LIF) to study the dynamics of $O(^1D)$ reactions with isotopically labeled alcohols at room temperature and 10 Torr. They found that approximately 70% of the OH production originated from the methanol hydroxyl position. In other words, the primary site of $O(^1D)$ attack upon the alcohols is the O–H bond. Matsumi et al. was the first one to measure rate constants and branching ratios for $O(^1D)$ reactions with CH_3OH. By measuring temporal profiles of the reactant and product atoms with vacuum-UV laser-induced fluorescence (VUV-LIF) method at 115.2 nm,[23] the total rate constant was determined as (5.1 ± 0.1) × 10^{-10} cm^3 molecule^{-1} s^{-1} at 300 K and 1–2 Torr (detailed information is listed in Table 1). Huang et al. predicted the total rate coefficient as 4.8 × 10^{-10} cm^3 molecule^{-1} s^{-1} at 300 K[24] using the potential-energy surface (PES) calculation. Following different primary channels of $O(^1D) + CH_3OH$, $O(^1D)$, sensitized HO_2 kinetics proceeds with reactions:

$$CH_2OH + O_2 \longrightarrow HO_2 + CH_2O$$

$$H_2O_2 + CH_3O \longrightarrow HO_2 + CH_3OH$$

$$HO_2 + HO_2 \longrightarrow H_2O_2 + O_2.$$

Clearly, HO_2 is formed through the reaction of fuel radicals (e.g., CH_2OH) with O_2 while CH_2OH is originated from the $O(^1D)$ insertion reaction into the C–H bond. The subsequent HO_2 consumption by fuel and intermediate species (e.g., CH_2O) plays a key role in fuel oxidation chemistry and atmospheric chemistry.

Yet another simple alcohol, also known as a promising alternative biofuel,[12] ethanol, has been rarely discussed for reaction rate constants and branching ratios for $O(^1D)$ reactions to authors' knowledge. Although Goldstein and Wiesenfeld mentioned possible reaction channels for $O(^1D) + C_2H_5OH$,[22] no explicit measurements were performed for this elementary reaction. Besides, few previous studies integrated a suite of selective and sensitive in situ time-resolved spectroscopic diagnostics for important intermediates including OH, HO_2, and H_2O in such $O(^1D)$ kinetic studies, which greatly impair the understanding of the $O(^1D)$ reaction with ethanol and the subsequent $O(^1D)$ sensitized HO_2 kinetics.

Laser-based time-resolved diagnostics, including ultraviolet (UV) and mid-infrared (IR) direct absorption spectroscopy (DAS), LIF, and cavity ring-down spectroscopy, have been applied for radical species detection in the past decades.[27–35] However, these traditional methodologies have limitations for the study of $O(^1D)$-sensitized HO_2 kinetics. For example, in LIF, HO_2 is measured indirectly through chemical conversion to OH. Unexpected HO_2 reactions, fluorescence quenching or OH detection uncertainty will all bring additional experimental uncertainties.[30] DAS is a powerful spectroscopic technique that can provide sensitive detection if a strong transition is targeted in a spectral region free of interference. However, "contamination-free" spectral region for the target species may be unrealistic for HO_2 due to the absorption from H_2O_2, H_2O, and larger fuels with broadband spectral features in mid-IR or UV regions.[34,35] To this end, we propose Faraday rotation spectroscopy[36–38] as a robust methodology for HO_2 measurements in this study.

Faraday rotation spectroscopy (FRS) was first applied for HO_2 detection by Brumfield et al.[36] at Princeton. The HO_2 detection limit was improved by FRS with a modulated magnetic field, but no time-dependent measurements were attempted due to the slow B-field modulation. Recently, Teng et al.[37,38] and Zhong et al.[39]

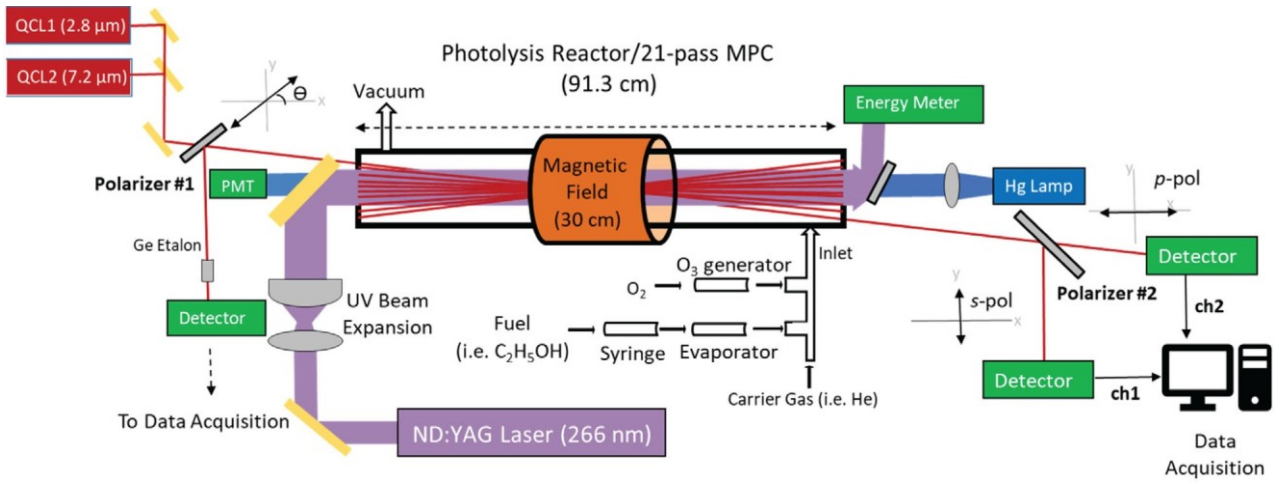

FIGURE 1 Experimental setup schematic [Color figure can be viewed at wileyonlinelibrary.com]

demonstrated the application of line-scanned FRS for quantitative and time-resolved measurements of HO_2 in $O(^1D)$ and HO_2 kinetic studies. Yan et al.[40] and Zhong et al.[26] discussed the branching ratios of $O(^1D)$ reactions with fuels in plasma-assisted combustion and some missing pathways for HO_2 formation using FRS, together with OH measurements from IR-DAS and O_3 measurements from UV-DAS. This well-developed diagnostic setup (introduced in the Experimental Section) provides a versatile system to study $O(^1D)$ reactions with complex fuels and the subsequent $O(^1D)$-sensitized kinetics.

In this work, we aim to study the multichannel dynamics of excited singlet oxygen atom $O(^1D)$ reactions with C_2H_5OH and the kinetics of subsequent reactions via selective and time-resolved detection of HO_2 using FRS. We also applied IR-DAS for OH and H_2O and UV-DAS for O_3. Absolute photolysis light was quantified by in situ actinometry. The proposed reaction channels, in analogy with those of $C_2H_5OH + O$,[41, 42] are shown below:

$$C_2H_5OH + O(^1D) \longrightarrow CH_3CHOH + OH \quad (R1)$$

$$\longrightarrow CH_2CH_2OH + OH \quad (R2)$$

$$\longrightarrow CH_3CH_2O + OH \quad (R3)$$

$$\longrightarrow CH_3O + CH_2OH. \quad (R4)$$

The paper is organized as follows: in the Experimental Section, the photolysis flow reactor, diagnostic methods, and the calibration of OH, HO_2 absolute concentrations will be discussed. In the Results and Discussion section, we will present time-resolved measurements of intermediate species OH, HO_2, and H_2O together with uncertainty and sensitivity analysis. The branching ratios of the reaction between $O(^1D)$ and ethanol will be fitted by an in-house reaction mechanism. Important $O(^1D)$-sensitized reaction pathways will be summarized. This study will fill the gap of knowledge of $O(^1D)$ reactions with oxygenated biofuels and $O(^1D)$-sensitized HO_2 kinetics. Further, it will promote the understanding of plasma-assisted biofuel oxidation and biofuel leakage in the atmosphere.

2 | EXPERIMENTAL SECTION

2.1 | Experimental setup

The experimental setup shown in Figure 1 is described in detail previously.[26, 37–40] Here we only provide a brief description. In all experiments, helium was used as the bath gas. The measurements were performed at 297 K and 60, 120, and 150 Torr.

The work was based on the Nd:YAG laser (Quantel Q-smart 850, 266 nm) photolysis coupled to the UV-IR DAS, and IR-FRS spectroscopic system. A quartz flow reactor with an inner diameter of 56 mm and a photolysis path-length of 913 mm was used. A pair of spherical mirrors with a focal length of 250 mm was installed at the both ends of the reactor. The mirror substrate was UV-grade CaF_2, offering over 90% transmittance for UV. A protective gold coating extends 8 mm from the edge of the mirror, leaving a 20° section transparent for the IR-DAS and IR-FRS detection. The uncoated central part of the spherical mirrors, 40 mm in diameter, allowed for the UV photolysis beam to pass through the cell and generate $O(^1D)$ atoms from O_3. The homogeneity of the laser beam was ensured by a beam expander along the photolysis pathway and a 22-mm i.d. apertures at the entrance of the reactor. At the exit, a high-energy pyroelectric sensor (Ophir, PE50BF-DIF-C) was placed to monitor the laser photon fluence. The

absolute photon flux was determined quantitatively using in situ actinometry. A repetition rate of 0.4 Hz was applied to the Nd:YAG laser to satisfy slow flow conditions and ensure the entire replacement of the gas volume between laser pulses.

The photolysis reactor also served as a Herriot multi-pass cell (MPC) with 21 passes for two quantum cascade lasers (QCL) emitting in the mid-IR (7.2 μm, Thorlabs; and 2.8 μm, Nanoplus). An axial magnetic field (ca. 380 G at the center of the reactor) was generated by a 300-mm long solenoid with DC current for IR-FRS measurements. With 21 passes through the reactor and considering the overlap between the QCLs and UV beam, the effective pathlength of the IR-FRS signals was 6.3 m (limited by solenoid length) while that of the IR-DAS signal was 7.5 m.

2.2 | In situ actinometry and O(^{1}D) measurements

To determine the branching ratio of the target reaction as O(^{1}D) + C_2H_5OH, an accurate quantification of O(^{1}D) concentrations was critical. In this work, we applied in situ laser light actinometry to determine the photon flux F (photons cm^{-2}) and further the absolute concentration of O(^{1}D). Discussions of this technique can be found elsewhere.[35,40] In the photolysis of O_3/O_2/He mixtures at 60 Torr, 297 K, the UV-DAS signals at 253.65 nm is monitored by an imaging spectrometer (Acton 2500i) together with a photomultiplier tube (Hamamatsu R7154) with an amplifier (Hamamatsu C6271). The cross section of O_3 at this monitoring wavelength (253.65 nm) was characterized previously.[43] With this detailed characterization of the absorption cross section and the photolysis light path of 913 mm, the two-stage decay of the O_3 concentration is shown in Figure 2. The first stage was the direct photolysis O_3 depletion:

$$O_3 + h\nu \longrightarrow O(^1D) + O_2 \quad \text{(P1a)}$$

$$\longrightarrow O(^3P) + O_2. \quad \text{(P1b)}$$

In the second stage, O_3 interacted with excited oxygen atoms O(^{1}D) and excited oxygen molecules $O_2(^1\Sigma)$:

$$O(^1D) + O_2 \longrightarrow O(^3P) + O_2(^1\Sigma)$$

$$O_2(^1\Sigma) + O_3 \longrightarrow O(^3P) + 2O_2$$

$$O(^1D) + O_3 \longrightarrow 2O_2.$$

Photon fluence F (photons cm^{-2}) was determined by fitting the experimental temporal profiles of O_3 with numerical simulations from a small reaction mechanism (see the Supporting Information). The actinometry measurements were performed before the kinetic measurements of O(^{1}D) + C_2H_5OH. During the measurements, the readout of the pyroelectric detector measuring the laser pulse energy was recorded and then used to introduce proper corrections for the drift of the photon fluence. For all experimental conditions, the photolysis laser photon fluence inside the reactor was varied in the range (1.7–2.7) × 10^{16} photon cm^{-2} pulse^{-1}.

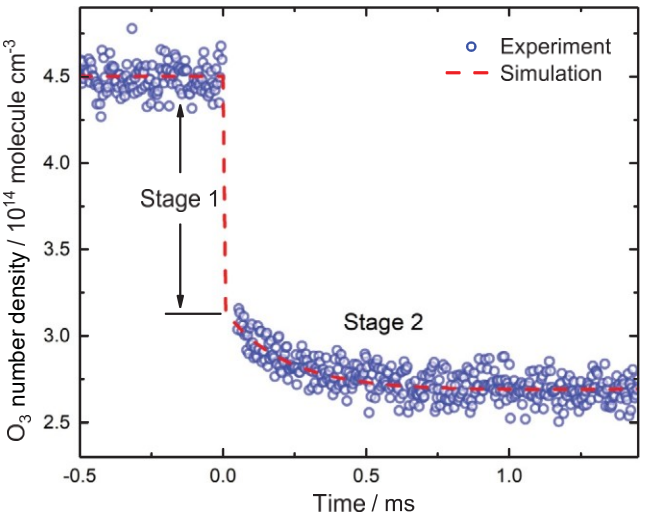

FIGURE 2 In situ actinometry based on O_3 depletion of the O_2/O_3/He mixture at 60 Torr and 297 K. O_3 is monitored at the wavelength of 253.65 nm (mercury line). The red line is fitted by an in-house mechanism where photon fluence (photons cm^{-2}) is the fitting parameter. The initial O_2 number density is 2.04 × 10^{16} molecule/cm^3 [Color figure can be viewed at wileyonlinelibrary.com]

2.3 | Faraday rotation spectroscopy and HO_2 measurements

Paramagnetic species HO_2 plays an important role in the kinetics of the target reaction O(^{1}D) + C_2H_5OH. In the presence of the paramagnetic species HO_2 and an external magnetic field, magnetically induced circular birefringence will lead to the rotation of the polarization plane of linearly polarized light and sensitive and selective HO_2 diagnostics. In this work, the time-resolved FRS signals of HO_2 radicals were measured at the spectral region around 1396.91 cm^{-1} (7.2 μm), which is a Q-branch spectral feature for a vibrational transition. Figure 1 shows the balanced-detection IR-FRS configuration. A pair of wire-grid polarizers (labeled as Polarizer #1 and #2) are used before and after the MPC. Polarizer #1 polarizes the incident light, and Polarizer #2 serves as an analyzer to convert laser polarization rotation into intensity changes. Specifically, the axis of Polarizer #2 is rotated at an angle of

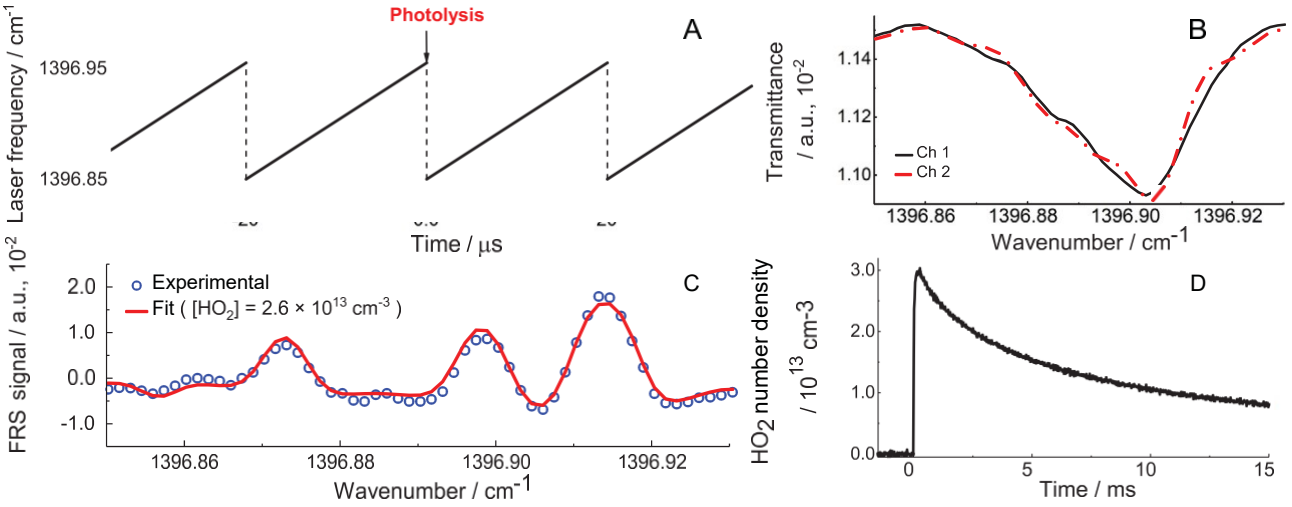

FIGURE 3 An illustration of the line-scanned FRS. (A) Continuous linear laser frequency scanning at a rate of 50 kHz from 1396.85 to 1396.95 cm^{-1}. Consecutive spectra were recorded with UV photolysis initiated after the second scan. (B) Sample transmittance signals from two channels (ch1 and ch2 in Figure 1) after digital balancing. The differences between two channels lead to HO_2 FRS signals. (C) A sample FRS spectrum of HO_2 with external magnetic field of 380 G. Least-means-squares fitting using HITRAN parameters was also provided. (D) A sample profile of HO_2 measured by FRS at 297 K and 60 Torr. The shaded area indicates the fitting uncertainty [Color figure can be viewed at wileyonlinelibrary.com]

45° with respect to Polarizer #1, hence the exit beam is split into s and p orthogonal polarizations in the transmitted and reflected beams. The light intensity of two beams is detected using photodetectors (VIGO, PVI-4TE-8) and the differential measurements between s and p polarizations lead to FRS signals. Common-mode intensity noise (including shared absorption features from nonparamagnetic species H_2O_2, C_2H_5OH, etc.) will be suppressed given that proper balancing is performed.[37,38]

The line-scanned FRS scheme is further demonstrated in Figure 3. Figure 3(A) shows the saw-tooth laser frequency scanning scheme across the target HO_2 transition at a rate of 50 kHz, leading to an acquisition time of 20 μs for each spectrum. Figure 3(B) presents the directly measured transmittance around the target spectrum region, where absorption signals from ethanol and other species are clear. However, the spectral interference was effectively suppressed using IR-FRS, shown as FRS signals in Figure 3(C). A time-resolved profile of HO_2 is shown in Figure 3(D). With O_3 photolysis and $O(^1D)$ production initiated at "time zero," there was a prompt generation of HO_2 and a subsequent decay controlled by the $O(^1D)$-sensitized HO_2 kinetics.

The absolute concentration of HO_2 radicals determined from IR-FRS was calibrated based on a well-studied mechanism in the $CH_3OH/(COCl)_2/O_2/He$ mixtures.[44] The precursor, oxalyl chloride, $(COCl)_2$, has been a clean Cl atom source in various kinetic studies. At 266 nm, the major channel of oxalyl chloride photolysis reaction was reaction (P2), which produced Cl atoms via the photon-dissociation reaction. HO_2 was further produced from the subsequent reaction between Cl atom and methanol in the presence of excessive O_2 molecules:

$$(COCl)_2 + h\nu\ (266\ \text{nm}) \longrightarrow 2CO + 2Cl \qquad \text{(P2)}$$

$$Cl + CH_3OH \longrightarrow HCl + CH_2OH$$

$$CH_2OH + O_2 \longrightarrow HO_2 + CH_2O.$$

All the related reactions for the HO_2 calibration were included in a small mechanism. With initial concentrations of $(COCl)_2$, CH_3OH, O_2 and photon fluence known, the absolute concentration of HO_2 could be predicted from the mechanism. This calibration experiment connected FRS signals and absolute HO_2 yield for a given condition, laying the foundation for the determination of HO_2 concentrations in the following experiments. A sample calibration result is provided in the Supporting Information.

2.4 | Direct absorption spectroscopy and OH, H_2O measurements

To better capture the subsequent kinetics, another QCL targeting at 2.8 μm was used for measuring time-resolved concentrations of OH and H_2O generated during the reactions following ozone photolysis. The target spectral region for OH is ca. 3568.52 cm^{-1} while that of H_2O is ca. 3568.29 cm^{-1}. During the measurements, the maximum QCL laser frequency fluctuations were observed to be ca. 3×10^{-3}

TABLE 2 Experimental conditions and results. T = 297 K. All concentrations are given in units of molecule cm^{-3}, photon fluence Φ in photons cm^{-2}. ϕ_1–ϕ_4 refer to the fitted branching ratios of four reaction channels (R1–R4)

No	P (Torr)	$[C_2H_5OH]_0$ ($\times 10^{15}$)	$[O_2]_0$ ($\times 10^{16}$)	$[O_3]_0$ ($\times 10^{14}$)	$[O(^1D)]_0$ ($\times 10^{14}$)	$[O]_0$ ($\times 10^{13}$)	$[\Phi]$ ($\times 10^{16}$)	ϕ_1	$\phi_2 + \phi_3$	ϕ_4
1	60	5.41	1.13	1.14	0.56	0.63	1.88	0.70	0.00	0.30
2	60	5.40	1.50	0.68	1.49	1.66	2.37	0.39	0.09	0.52
3	60	10.80	1.50	1.13	1.09	1.21	2.73	0.41	0.11	0.48
4	60	8.61	3.30	5.95	1.43	1.59	2.50	0.42	0.14	0.44
5	60	8.61	3.30	6.05	1.35	1.50	2.21	0.51	0.09	0.40
6	60	8.61	3.30	5.90	1.48	1.64	2.41	0.41	0.16	0.43
7	120	8.76	3.35	5.87	1.62	1.80	2.44	0.35	0.22	0.43
8	120	8.76	3.35	5.85	1.64	1.82	2.58	0.49	0.11	0.40
9	120	8.76	3.35	6.57	1.00	1.10	2.34	0.45	0.09	0.46
10	150	10.90	1.53	1.19	1.06	1.18	2.11	0.38	0.30	0.32
11	150	5.54	1.15	0.82	0.86	0.96	1.72	0.54	0.10	0.36
12	150	5.47	1.15	1.14	0.58	0.64	1.93	0.45	0.10	0.45

cm^{-1} at the pressure range from 60 to 150 Torr, which was four times smaller than the full width at half maximum of OH absorption profiles according to HITRAN simulations. Therefore, we applied DAS for detecting both OH and H_2O and assumed insignificant spectral interference between the OH and H_2O concentration retrieval.

The absorption cross section of the OH radical at 3568.52 cm^{-1} was calibrated using well-studied chemical reactions $O_3 + h\nu(266nm) \longrightarrow O(^1D) + O_2$ and $O(^1D) + H_2O \longrightarrow 2OH$. The method was discussed in previous publications,[40] and the measured absorption cross section in this work was $\sigma_{OH} = (3.75 \pm 0.31) \times 10^{-18}$ cm^2 $molecule^{-1}$ at 60 Torr and $(2.30 \pm 0.21) \times 10^{-18}$ cm^2 $molecule^{-1}$ at 120 Torr. The absorption cross section of H_2O at 3568.29 cm^{-1} used in this work is $\sigma_{H_2O} = (2.45 \pm 0.25) \times 10^{-19}$ cm^2 $molecule^{-1}$ at 60 Torr and $(1.26 \pm 0.15) \times 10^{-19}$ cm^2 $molecule^{-1}$ at 120 Torr.

2.5 | Reagents and experimental conditions

The gas flow rates were controlled by well-calibrated mass flow controllers (MKS instruments). The gases He (99.999%, ultra high purity , Airgas) and O_2 (99.5%, Airgas) were used as supplied. O_3 was produced by an ozone generator (Ozone Solutions, TG-20) from the downstream of O_2 flow. Ethanol (≥99.9%, Fisher Scientific) was delivered by a precision syringe pump (KdScientific, Legato 110) through a central capillary tube (200 μm) into a prevaporization chamber with a flow rate of 0.02–0.04 mL/min.

The experimental conditions are listed in Table 2. The total flow rates of the reactant mixtures with helium were in the range of 2000–5050 sccm (standard cubic centimeters per minute). The initial concentrations of the reactants used were (1.1–3.5) × 10^{16} molecules cm^{-3} (O_2), (0.7–6.6) × 10^{14} molecules cm^{-3} (O_3), and (5.4–10.9) × 10^{15} molecules cm^{-3} (C_2H_5OH).

3 | RESULTS AND DISCUSSION

To determine the branching ratio of the target reaction and discuss the kinetics, an in-house reaction mechanism was developed (provided in Table 3). Then, transient profiles of OH and H_2O from IR-DAS and those of HO_2 from IR-FRS were fitted by numerical simulations of the differential equation systems corresponding to this reaction mechanism using SCIENTIST software.[45] In the mechanism, reactions of electronically excited species including atomic oxygen $O(^1D)$ and molecular oxygen $0_2(^1\Sigma)$, radicals including OH, O, H, HO_2, H_2O_2, CH_2OH, CH_3O, CH_3CHOH, CH_2CH_2OH, CH_3CH_2O, $O_2CH_2CH_2OH$, and C_2H_5OO, and stable molecules including O_2, O_3, H_2O, CH_3CHO, and C_2H_5OH were considered. As the diffusion timescale for major radicals and atoms out of photolysis beam (50–100 ms) is more than five times larger than the half-life of HO_2 radicals (ca. 5 ms) and almost two orders longer compared with OH radical decay time (ca. 1 ms), the diffusion effect in the photolysis reactor was insignificant. Simulated and measured profiles of OH, HO_2 and H_2O are shown in Figure 4–6. The direct reaction of $O(^1D)$ with C_2H_5OH is fast and dominant in the current kinetic system. The timescale of this reaction is less than 1 μs. Therefore, we treat this reaction different from other secondary reactions.

TABLE 3 The in-house mechanism for $C_2H_5OH + O(^1D)$ kinetic study. R = 8.314 J/mol K. Rate constant unit: cm^3/molecules

No.	Reaction	Rate constant	Reference	$\partial \ln \phi_4 / \partial \ln k_i$[a]	$\partial \ln(\phi_2 + \phi_3) / \partial \ln k_i$
1	$C_2H_5OH + O(^1D) \longrightarrow CH_3CHOH + OH$	$(0.46 \pm 0.12) \times 3 \times 10^{-10}$	This work[b]	4.027	2.231
2	$C_2H_5OH + O(^1D) \longrightarrow CH_2CH_2OH + OH$	$(0.12 \pm 0.03) \times 3 \times 10^{-10}$	This work	2.414	0.744
3	$C_2H_5OH + O(^1D) \longrightarrow CH_3CH_2O + OH$		This work[c]	0.231	0.818
4	$C_2H_5OH + O(^1D) \longrightarrow CH_3O + CH_2OH$	$(0.42 \pm 0.11) \times 3 \times 10^{-10}$	This work	1.410	0.966
5	$O(^1D) + O_2 \longrightarrow O + O_2(\Sigma)$	$2.64 \times 10^{-11} \exp(55/T)$	51	0.0778*	0.0853*
6	$O(^1D) + O_2 \longrightarrow O + O_2$	$0.66 \times 10^{-11} \exp(55/T)$	51	0.0225*	0.0213*
7	$O(^1D) + O_3 \longrightarrow O + O + O_2$	1.2×10^{-10}	51	0.0105*	0.0125*
8	$O(^1D) + O_3 \longrightarrow O_2 + O_2$	1.2×10^{-10}	51	0.00378	0.00743
9	$O_2(\Sigma) + O_2 \longrightarrow$ Products	3.9×10^{-17}	51	4.58e−4	1.42e−4
10	$O_2(\Sigma) + O_3 \longrightarrow O + 2O_2$	$3.63 \times 10^{-11} \exp(960/RT)$	52	4.58e−4	2.83e−5
11	$O_2(\Sigma) + H_2O \longrightarrow O_2 + H_2O$	$4.52 \times 10^{-12} \exp(740/RT)$	52	2.58e−4	2.83e−5
12	$O_2(\Sigma) + O \longrightarrow$ Products	8.0×10^{-14}	51	4.58e−4	2.83e−5
13	$OH + OH \longrightarrow H_2O + O$	$1.07 \times 10^{-12}(1+10^{-4}(T-483)^2)^{0.2}$	53	1.21e−5	8.54e−5
14	$OH + OH \longrightarrow H_2O_2$	$k_0 = 9.0 \times 10^{-31}(T/300)^{-3.5}$, $k_\infty = 2.4 \times 10^{-11}(T/300)^{-0.5}$ $Pr = k_0[M]/k_\infty$ $\log F = \frac{\log_{10} F_{cent}}{1+f_1^2}$ $(F_{cent}=0.37)$ $k = k_\infty \frac{Pr}{1+Pr} F$	54	4.58e−4	5.66e−4
15	$OH + CH_3CH_2OH \longrightarrow H_2O + CH_3CHOH$	3.00×10^{-12}	55	0.0998*	0.0309*
16	$OH + CH_3CH_2OH \longrightarrow H_2O + CH_2CH_2OH$	2.61×10^{-13}	55	0.0158*	0.0268*
17	$OH + O \longrightarrow O_2 + H$	$2.4 \times 10^{-11} \exp(109/T)$	56	0.0188*	0.00122
18	$OH + O \longrightarrow HO_2$	$[M]1.6 \times 10^{-31}(T/298)^{-2.6}$	Estimated from OH + H	0.00855	1.13e−4
19	$OH + H \longrightarrow H_2 + O$	$6.86 \times 10^{-14}(T/298)^{2.8} \exp(-1950/T)$	57	4.58e−4	5.66e−5
20	$OH + H \longrightarrow H_2O$	$[M]1.6 \times 10^{-31}(T/298)^{-2.6}$	58	4.58e−4	2.83e−5
21	$OH + H_2O_2 \longrightarrow H_2O + HO_2$	$2.9 \times 10^{-12} \exp(-109/T)$	59	3.58e−4	1.13e−4
22	$OH + HO_2 \longrightarrow H_2O + O_2$	$2.4 \times 10^{-11} \exp(250/T)$	60	0.0304*	0.0329*
23	$O + HO_2 \longrightarrow O_2 + OH$	$1.35 \times 10^{-11} \exp(1860/RT)$	56	0.0392*	0.0943*
24	$O + H_2O_2 \longrightarrow OH + HO_2$	$1.40 \times 10^{-12} \exp(-16{,}630/RT)$	56	3.58e−5	5.66e−5
25	$H + HO_2 \longrightarrow H_2 + O_2$	$7.11 \times 10^{-11} \exp(-5900/RT)$	61	5.06e−4	5.11e−4
26	$H + HO_2 \longrightarrow 2O_H$	$2.81 \times 10^{-10} \exp(-3660/RT)$	61	0.00688	0.00509
27	$H + HO_2 \longrightarrow H_2O + O$	$5.00 \times 10^{-11} \exp(-7200/RT)$	61	2.85e−4	9.07e−4
28	$H + HO_2 \longrightarrow O(^1D) + H_2O$	$3.29 \times 10^{-12}(T/298)^{1.55} \exp(670/RT)$	62	4.58e−4	2.55e−4
29	$O + O_2 \longrightarrow O_3$	$[M]3.4 \times 10^{-34}(T/300)^{-1.2}$	63	8.65e−4	0.0025
30	$H + O_2 \longrightarrow OH + O$	$1.62 \times 10^{-10} \exp(-62{,}110/RT)$	64	3.04e−4	2.83e−4
31	$H + O_2 \longrightarrow HO_2$	$[M]5.4 \times 10^{-32}(T/298)^{-1.8}$	65	0.0258*	0.0211*
32	$OH + O_3 \longrightarrow HO_2 + O_2$	$1.7 \times 10^{-12} \exp(-7820/RT)$	56	0.00345	0.0171*
33	$O + O_3 \longrightarrow O_2 + O_2$	$8.0 \times 10^{-12} \exp(-17130/RT)$	66	6.05e−5	3.68e−4
34	$H + O_3 \longrightarrow OH + O_2$	$1.4 \times 10^{-10} \exp(-3990/RT)$	67	0.0488*	0.0205*
35	$HO_2 + O_3 \longrightarrow OH + O_2 + O_2$	$1.97 \times 10^{-16}(T/298)^{4.57} \exp(5760/RT)$	56	0.00101	0.00334
36	$HO_2 + HO_2 \longrightarrow H_2O_2 + O_2$	$2.86 \times 10^{-13} \exp(4990/RT)$	56	0.0182*	0.00995
37	$CH_2OH + O_2 \longrightarrow CH_2O + HO_2$	0.95×10^{-11}	66	0.0865*	0.0504*
38	$CH_3CHOH + O_2 \longrightarrow CH_3CHO + HO_2$	1.90×10^{-11}	66	0.00673	0.00123
39	$CH_3O \longrightarrow CH_2OH$	$1.0 \times 10^{13} \exp(-109{,}000/RT)$	68	4.53e−5	2.83e−5
40	$CH_3O \longrightarrow CH_2O + H$	$9.0 \times 10^{-11} \exp(-56{,}460/RT)$	64	6.05e−5	1.13e−4
41	$CH_3O + H_2O_2 \longrightarrow CH_3OH + HO_2$	$5.0 \times 10^{-15} \exp(-10{,}810/RT)$	69	4.58e−4	6.05e−4

(Continues)

TABLE 3 (Continued)

No.	Reaction	Rate constant	Reference	$\partial \ln \phi_4 / \partial \ln k_i$[a]	$\partial \ln(\phi_2 + \phi_3) / \partial \ln k_i$
42	$CH_3O + HO_2 \longrightarrow CH_2O + H_2O_2$	5.0×10^{-13}	57	0.00452	0.00144
43	$CH_3O + CH_3O \longrightarrow CH_3OH + CH_2O$	3.85×10^{-11}	70	4.55e-4	0.00151
44	$CH_3O + CH_3O \longrightarrow (CH_3O)_2$	3.0×10^{-12}	57	8.05e−5	2.83e−5
45	$CH_3O + OH \longrightarrow CH_2O + H_2O$	3.0×10^{-11}	57	4.23e−5	1.13e−4
46	$CH_3O + O \longrightarrow CH_2O + OH$	1.0×10^{-11}	69	0.00141	0.00199
47	$CH_3O + O \longrightarrow CH_3 + O_2$	2.5×10^{-11}	71	0.00258	0.00851
48	$CH_3O + H \longrightarrow CH_2O + H_2$	3.3×10^{-11}	57	2.57e−4	2.55e−4
49	$CH_3O + H \longrightarrow CH_3 + OH$	3×10^{-11}	72	4.21e−4	8.51e−5
50	$C_2H_5OH + O \longrightarrow CH_3CHOH + OH$	5.21×10^{-14}	73	0.0477*	0.0341*
51	$CH_3CHOH + O \longrightarrow CH_3CHO + OH$	1.5×10^{-10}	74	0.00921	0.00612
52	$CH_3CHO + OH \longrightarrow$ Products	1.63×10^{-11}	61	2.65e−4	2.83e−5
53	$CH_3CHO + O \longrightarrow$ Products	5.07×10^{-13}	75	1.72e−4	4.53e−4
54	$CH_2CH_2OH + H \longrightarrow$ products	8.3×10^{-11}	76	0.00101	3.11e−4
55	$CH_2CH_2OH + O_2 \longrightarrow O_2CH_2CH_2OH$	3.0×10^{-13}	66	0.00253	1.41e−4
56	$CH_2CH_2OH + CH_2CH_2OH \longrightarrow$ products	5.6×10^{-11}	77	2.95e−4	5.67e−4
57	$CH_3CH_2O + H \longrightarrow CH_3 + CH_2OH$	6.84×10^{-11}	78	0.00691	0.00125
58	$CH_3CH_2O + O_2 \longrightarrow CH_3CHO + HO_2$	9.48×10^{-15}	66	0.00212	0.00372
59	$CH_3CH_2O + C_2H_5OO \longrightarrow CH_3CHO + CH_3CH_2OOH$	1.54×10^{-11}	79	0.00394	0.00289
60	$CH_2CH_2OH + O \longrightarrow$ products	3×10^{-11}	estimated	0.00576	0.00377
61	$O_2CH_2CH_2OH + HO_2 \longrightarrow$ products	7×10^{-12}	this work	0.103*	0.0813*

[a]The last two columns are sensitivities, defined as $\frac{\delta \ln \phi}{\delta \ln k_i}$ in Equationn (2). k_i is reaction rate for reaction i. ϕ is the branching ratio shown in Table 4.* denotes the important reactions as discussed in Results and Discussions.

[b] As this reaction occurs at a microsecond timescale, we estimated the rate constant as 3×10^{-10} and only determined the branching ratio.

[c]According to our discussion, reactions (2) and (3) cannot be distinguished. Therefore, only a total branching ratio of reactions (2) and (3) is provided here.

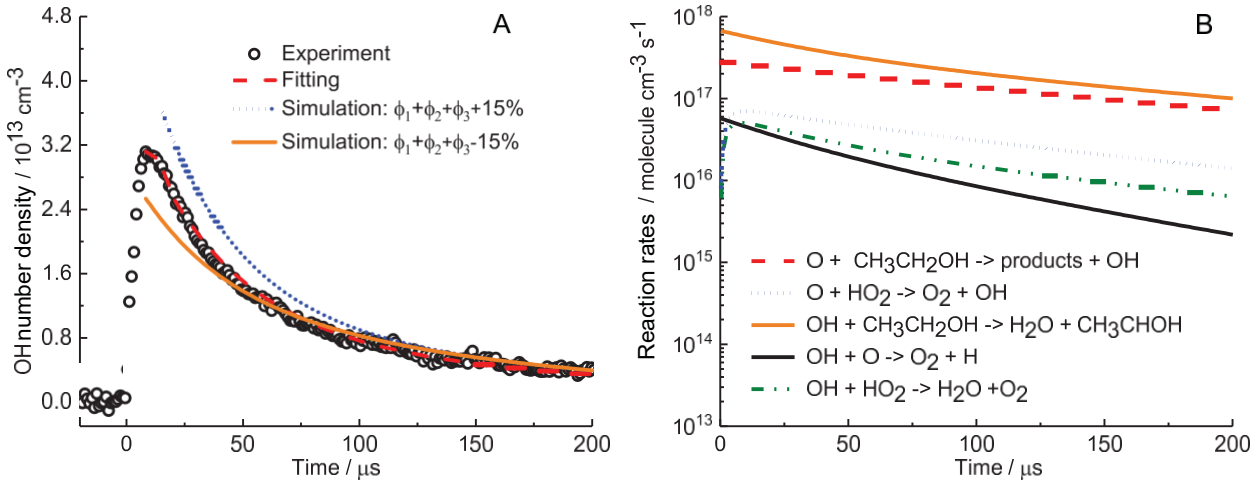

FIGURE 4 Left: OH time history measured by IR-DAS at 2.8 μm with numerical fitting to experimental data. The initial rise of OH is strongly interfered with the electronic noise, and thus we only fit the OH decay profile. Two other simulations with branching ratios ±15% for OH channels are also presented. Right: The time evolution of reaction rates for dominant reactions (except the target reaction $O(^1D) + C_2H_5OH$) of OH calculated by the reaction mechanism. The reaction condition for both plots is No. 8 in Table 2 [Color figure can be viewed at wileyonlinelibrary.com]

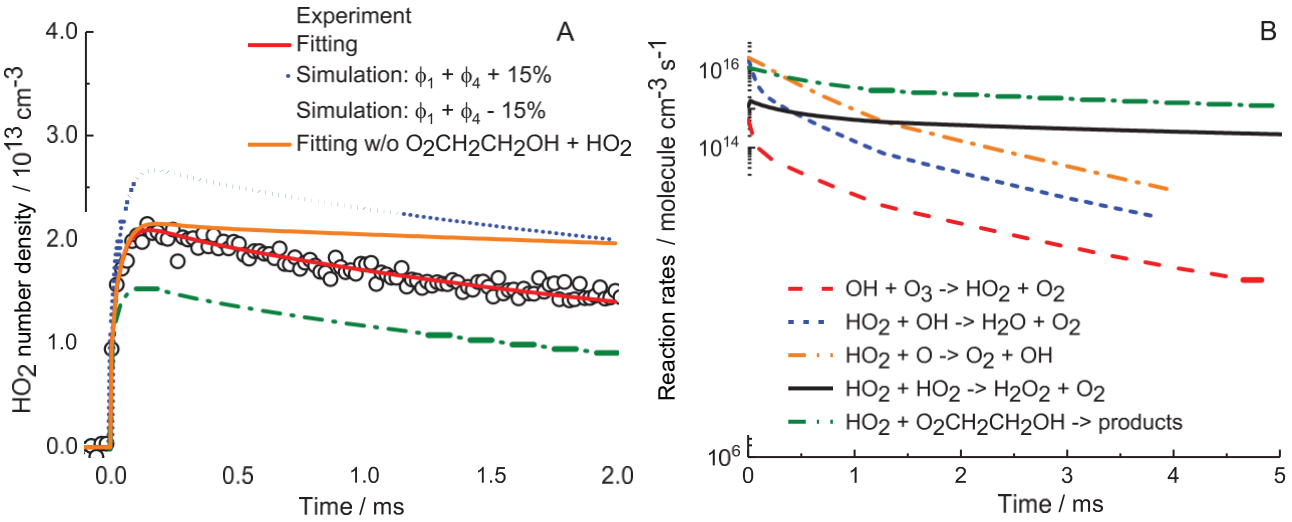

FIGURE 5 (A) HO_2 time history measured by IR-FRS at 7.2 μm with numerical fitting to experimental data. Two other simulations with branching ratios ±15% for HO_2 channels are shown with dotted and dashed lines. The simulation without one HO_2 consumption channel as $O_2CH_2CH_2OH + HO_2$ is also presented in the solid yellow line. (B) The time evolution of reaction rates for dominant reactions of HO_2 in the millisecond timescale calculated by the reaction mechanism. The reaction condition for all plots is No. 7 in Table 2 [Color figure can be viewed at wileyonlinelibrary.com]

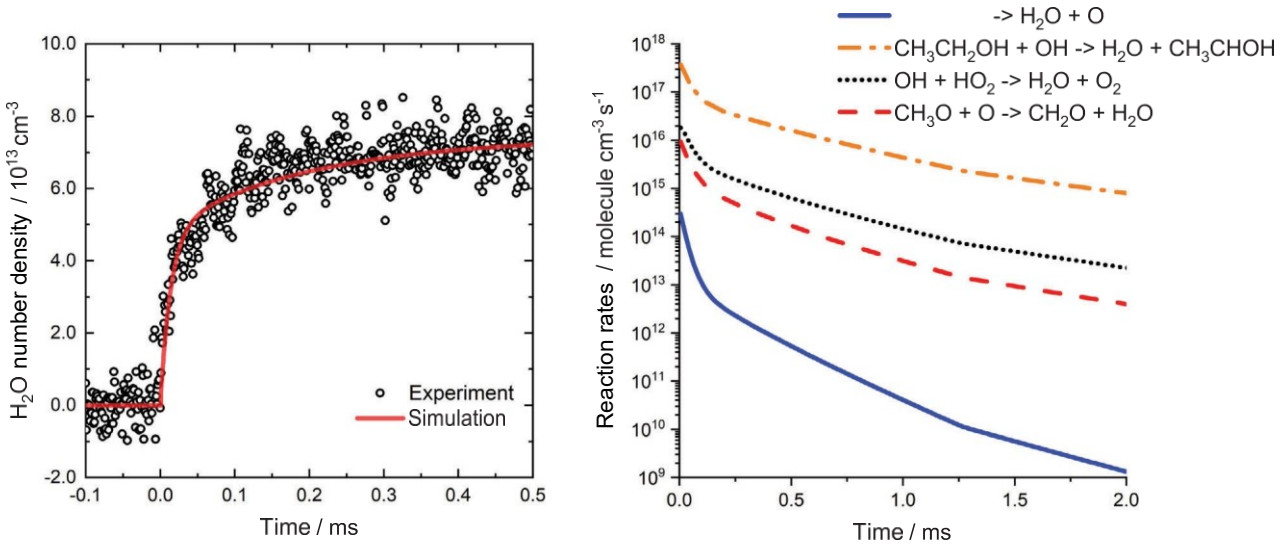

FIGURE 6 (A) H_2O time history measured by IR-DAS at 2.8 μm with the numerical simulation from the reaction mechanism at room temperature and 120 Torr. Reaction condition is No. 9 in Table 2. (B) The time evolution of reaction rates for dominant reactions of H_2O in the millisecond timescale calculated by the reaction mechanism. The reaction condition for both plots is No. 9 in Table 2 [Color figure can be viewed at wileyonlinelibrary.com]

The dominant sources of uncertainty in the current measurements stem from the uncertainty of OH and HO_2 concentrations. Uncertainties in the OH cross sections and uncertainties in the OH absorption length are folded into an total uncertainty of 10%. Our previous work[40] indicated an uncertainty of 16% in the OH measurements. Such a discrepancy may originate from the improvement of the optical alignment and better tuning of the laser conditions. The FRS measurements of HO_2 significantly reduce its associated uncertainty as FRS better suppresses the spectral interference and background noise. The uncertainty associated with the magnetic field strength and the pathlength contributes as much as 3% to the HO_2 uncertainty. The uncertainty associated with FRS calibration, FRS modeling, and spectrum fitting at these conditions typically does not exceed 5%. The overall uncertainties for HO_2 measurements are estimated as 8% in this work.

Sensitivity analysis has been carried out for all reactions in the mechanism and listed in Table 3 using a representative experimental profile (Experimental condition 12 in Table 2). Among the reactions included in the mechanism, some are highly sensitive to the branching ratio, while some have marginal influence. Using the sensitivity coefficient exceeding 10^{-2} as a criterion of reaction importance, one can identify important reactions for each branching ratio. For example, the following reactions were selected as important (labeled in Table 3 with asterisks) for the branching ratio ϕ_4: reactions 5–7, 15–17, 22, 23, 31, 34, 36, 37, 50, and 61. Assigning errors of ±15% for the well-studied reactions (reactions 5–7, 15, 16, 22, 31, 36, 37) and ±25% for the rest of those important reactions, and assuming statistical independence of their errors, we calculated the error in the target branching ratio ϕ_4 as 12.2% contributed by the mechanism. The error for other branching ratios contributed by the mechanism can be calculated with the same procedures.

For individual conditions listed in Table 2, the branching ratio is determined via a fitting process which involves both experimentally measured concentrations (denoted as $\boldsymbol{X}$) and mechanism-dependent reaction rate constants (denoted as $\boldsymbol{k}$). The branching ratio is formulated as

$$\phi = \phi(\boldsymbol{X}, \boldsymbol{k}). \tag{1}$$

The uncertainty of the branching ratio is

$$\frac{\Delta\phi}{\phi} = \sum_{i=1}^{\max(i)} \left(\frac{\partial \ln\phi}{\partial \ln X_i}\right)_{\text{mech}} \left(\frac{\Delta X_i}{X_i}\right)_{\text{exp}} + \sum_{j=1}^{\max(j)} \left(\frac{\partial \ln\phi}{\partial \ln k_j}\right)_{\text{mech}} \left(\frac{\Delta k_j}{k_j}\right)_{\text{mech}}, \tag{2}$$

which is a sum of experimental uncertainties from species measurements and mechanism uncertainties from related reactions, weighted by their sensitivities (the sensitivity of the individual reaction is listed in Table 3). As most reactions and species in the mechanism have negligible sensitivities (as discussed above), the calculation is simplified and tractable. For example, the sensitivity of the branching ratio ϕ_4 towards the species profiles of OH and HO_2 is estimated as 0.74 and 0.79. Given the uncertainty of OH and HO_2 measurements, the contributed error from the species measurements for the branching ratio ϕ_4 is 13.7%. Following Equation (2), the combined uncertainty for the branching ratio ϕ_4 is 25.9%. Similarly, the combined uncertainty for ϕ_1 is 25.8% and that for (ϕ_2 + ϕ_3) is 24.1%.

According to the proposed reaction channels (R1–R4), OH is one of the primary products of $O(^1D)$ + C_2H_5OH. With measured OH profiles at different conditions (a sample measurement is shown in Figure 4(A)), the OH production channels (R1–R3) and non-OH production channel (R4) are fitted to 0.58 ± 0.15 and 0.42 ± 0.11. A perturbation of the branching ratio of ±15% not only introduces higher or lower initial peaks for the OH profile but also greatly influences the subsequent OH decay rates within the initial 100 μs. Figure 4(B) presents the time evolution of reaction rates for other dominant reactions of OH. In addition to the reaction between the excited oxygen atom $O(^1D)$ and ethanol, reactions with the ground state oxygen atom O continue to generate OH radicals:

$$C_2H_5OH + O \longrightarrow OH + \text{products}$$

$$HO_2 + O \longrightarrow OH + O_2.$$

The subsequent OH formation is negligible compared to its consumption, which is dominantly controlled by C_2H_5OH + OH reactions:

$$CH_3CH_2OH + OH \longrightarrow H_2O + CH_3CHOH. \tag{R15}$$

This reaction promptly consumes almost all OH radicals within 1 ms and convert them to the α-hydroxyethyl (CH_3CHOH) and water. Other reactions pathways through O and HO_2 radicals (shown in Figure 4(B)) are playing a minor role in the OH consumption. The reaction kinetics proceeds after the microsecond reaction channels (R1–R4). Products including hydroxymethyl (CH_2OH) and α-hydroxyethyl (CH_3CHOH) continue to contribute in the $O(^1D)$-sensitized HO_2 kinetics.

HO_2 is one of the secondary products of $O(^1D)$+ C_2H_5OH. The initial HO_2 yield is directly sensitive towards the production of CH_2OH generated from the reaction channel (R4) and CH_3CHOH from the reaction channel (R1). The former one generates HO_2 via the oxidation reaction $CH_2OH + O_2 \longrightarrow HO_2 + CH_2O$, while the latter one via the reaction $CH_3CHOH + O_2 \longrightarrow HO_2 + CH_3CHO$. Therefore, by fitting to the time-resolved HO_2 profile, the branching ratios for HO_2 production channels (R1, R4) and non-HO_2 production channels (R2, R3) are determined as 0.88 ± 0.23 and 0.12 ± 0.03, respectively. A perturbation of the branching ratio of ±15% together with optimal fitting to a sample HO_2 measurement is shown in Figure 5(A). Even though HO_2 is a secondary product of the target reaction, the HO_2 profile is still offset by roughly 25% caused by this perturbation of the branching ratio. The above-mentioned HO_2 formation channels are shut down within the microsecond timescale. Only a minimal amount of HO_2 is formed via $OH + O_3 \longrightarrow HO_2 + O_2$ at the millisecond timescale, at which HO_2 decay rates are higher by several orders of magnitude (shown in Figure 5(B)). It is reported previously[46, 47] that low-temperature

TABLE 4 The branching ratios of the target reaction. The detailed mechanism is in Table 3

No	Reaction	Branching ratio
R1	$C_2H_5OH + O(^1D) \longrightarrow CH_3CHOH + OH$	$\phi_1 = 0.46 \pm 0.12$
R2	$C_2H_5OH + O(^1D) \longrightarrow CH_2CH_2OH + OH$	$\phi_2 + \phi_3 = 0.12 \pm 0.03$
R3	$C_2H_5OH + O(^1D) \longrightarrow C_2H_5O + OH$	
R4	$C_2H_5OH + O(^1D) \longrightarrow CH_3O + CH_2OH$	$\phi_4 = 0.42 \pm 0.11$

chain-branching pathways involving active species OH, O, HO_2 and particularly some oxygenated fuel radicals RO_2 contribute to the HO_2 decay. Reactions between simple oxygenated fuel radicals CH_3O_2[48] or $C_2H_5O_2$[49] and HO_2 have been discussed in detail. Nevertheless, a specific $HO_2 + RO_2$ reaction between HO_2 and $O_2CH_2CH_2OH$ (β-RO_2) at the low-temperature range is not understood well and poses a challenge in fitting the HO_2 decay in the current kinetic study. Based on the similar reaction between $CH_3CH_2O_2$ and HO_2, in this work we included the following reaction:

$$HO_2 + O_2CH_2CH_2OH \longrightarrow \text{Products} \qquad \text{(R61)}$$

with an estimated rate constant of 7×10^{-12} cm^3 $molecule^{-1}$ s^{-1}. $O_2CH_2CH_2OH$ (β-RO_2) is originated from a primary product of the reaction channel (R2) as CH_2CH_2OH (β-hydroxyethyl). CH_2CH_2OH is further oxidized (R55)[46, 50]:

$$O_2 + CH_2CH_2OH \longrightarrow O_2CH_2CH_2OH. \qquad \text{(R55)}$$

Ignoring the presence of $O_2CH_2CH_2OH$ and turning off reaction (R61) as the HO_2 consumption channel will dramatically postpone the decay of HO_2 in the discussed system (shown in Figure 5(A)). Clearly a detailed investigation is outside the scope of this work. High-level ab initio calculations and quantitative measurements of reaction kinetics of both HO_2 and RO_2 are required for a better characterization of the HO_2 kinetics.

From the above discussion, the interactions among reactive species result in the formation of stable molecules like H_2O. Reaction rates of dominant reactions of H_2O are plotted in Figure 6. Clearly, H_2O is generated mainly by the interactions between OH and HO_2. Therefore, H_2O transient profiles can be used to further validate the reaction mechanism and the proposed branching ratio. A sample profile of H_2O and the corresponding simulation are presented in Figure 6, which show a good agreement. Based on the mechanism, the major formation channel for H_2O is reaction (R15). As the OH yield at the microsecond timescale is completely controlled by the OH production channels (reaction R1–R3), the rapid formation of H_2O within 200 μs is directly correlated to the target $O(^1D)$ reaction. At a later stage, other reactions continue to generate H_2O:

$$OH + HO_2 \longrightarrow H_2O + O_2$$

$$CH_3O + O \longrightarrow HO_2 + CH_2O$$

$$OH + OH \longrightarrow H_2O + O.$$

To summarize, by measuring the transient profiles of HO_2, OH, and H_2O, we determine the branching ratios of the target reaction as the fitting parameters in the mechanism (summarized in Table 4). One missing low-temperature chain-branching reaction (R61) is also estimated for a better fitting of the experimental data. The unique $O(^1D)$ reaction kinetics of the target reaction is originated from the unique molecular structure of alcohols where a hydroxyl moiety is connected to a hydrocarbon chain. The presence of this hydroxyl moiety weakens the C–H bond, C–C bond, and C–O bond at the adjacent α-site,[46] such that a large fraction of reactive $O(^1D)$ can attack and insert into those positions (reaction R1, R3, and R4).

4 | CONCLUSION

In this work, the kinetics of $O(^1D)$ reactions with C_2H_5OH were investigated through quantitative time-resolved measurements of HO_2, OH, H_2O, and $O(^1D)$ in a photolysis flow reactor. Specifically, HO_2 was quantified by selective and time-resolved FRS, in which spectral interferences from nonparamagnetic hydrocarbon absorption were suppressed by the balanced-detection configuration. The branching ratios of $O(^1D)$ reactions with C_2H_5OH as well as its subsequent reaction kinetics were discussed in detail. Based on OH temporal profiles, the branching ratio of OH production channels was fitted to 0.58 ± 0.15. Moreover, HO_2 temporal profiles allow for the identification and estimation of the rate constant of a missing chain-branching reaction channel for HO_2 consumption involving $O_2CH_2CH_2OH$ (β-RO_2). Differing from $O(^1D)$ reactions with hydrocarbons, $O(^1D)$ reacts with alcohols by attacking and inserting into the adjacent α-site of the hydroxyl moiety. The work demonstrates the capability of the experimental apparatus combing IR-DAS, UV-DAS, with IR-FRS in the photolysis reactor for selective

measurements of low-temperature species (e.g., OH, HO_2, H_2O, and O_3) and kinetic studies of complicated chemical kinetics and dynamics involving $O(^1D)$ reaction with oxygenated fuels.

AC KNO WLEDGMENTS

This project is supported by the NSF grant CBET 1903362, DOE grant DE-SC0020233 of Plasma Science Center, Princeton SEAS innovation grant, ACEE center grant, and ExxonMobil research grant. HZ is grateful for support from Eli and Britt Harari Fellowship at Princeton University. HZ also acknowledges helpful discussions with Dazhi Xi from Department of Civil and Environmental Engineering at Princeton University on error and sensitivity analysis.

DATA AVAILABILITY S TATEMENT

Experimental data are available from the corresponding author upon reasonable request.

OR CID

Hongtao Zhong https://orcid.org/0000-0003-4064-6298
Chao Yan https://orcid.org/0000-0002-2415-6080

REFERENCES

1. Ju Y, Sun W. Plasma assisted combustion: dynamics and chemistry. *Prog Energy Combust Sci*. 2015;48:21–83.
2. Ju Y, Lefkowitz JK, Reuter CB, et al. Plasma Assisted low temperature combustion. *Plasma Chem Plasma Process*. 2016;36(1):85–105.
3. Yang S, Nagaraja S, Sun W, Yang V. Multiscale modeling and general theory of non-equilibrium plasma-assisted ignition and combustion. *J Phys D: Appl Phys*. 2017;50(43):433001.
4. Ravishankara AR, Hancock G, Kawasaki M, Matsumi Y. Photochemistry of ozone: surprises and recent lessons. *Science*. 1998;280(5360):60–61.
5. Azyazov VN, Heaven MC. Kinetics of active oxygen species with implications for atmospheric ozone chemistry. *Int J Chem Kinet*. 2015;47(2):93–103.
6. Gleit CE, Holland WD. Use of electrically excited oxygen for the low temperature decomposition of organic substances. *Anal Chem*. 1962;34(11):1454–1457.
7. Moss SJ, Jolly AM, Tighe BJ. Plasma oxidation of polymers. *Plasma Chem Plasma Process*. 1986;6(4):401–416.
8. Kim H-H, Ogata A, Futamura S. Oxygen partial pressure-dependent behavior of various catalysts for the total oxidation of VOCs using cycled system of adsorption and oxygen plasma. *Appl Catal, B*. 2008;79(4):356–367.
9. Ju Y, Reuter CB, Yehia OR, Farouk TI, Won SH. Dynamics of cool flames. *Prog Energy Combust Sci*. 2019;75:100787.
10. Burnham A, Han J, Clark CE, Wang M, Dunn JB, Palou-Rivera Ignasi. Life-cycle greenhouse gas emissions of shale gas, natural gas, coal, and petroleum. *Environ Sci Technol*. 2011;46(2):619–627.
11. Kerr RA. Natural Gas From shale bursts onto the scene. *Science*. 2010;328(5986):1624–1626.
12. Kohse-Höinghaus K, Oßwald P, Cool TA, et al. Biofuel combustion chemistry: from ethanol to biodiesel. *Angew Chem, Int Ed*. 2010;49(21):3572–3597.
13. Agarwal AK. Biofuels (alcohols and biodiesel) applications as fuels for internal combustion engines. *Prog Energy Combust Sci*. 2007;33(3):233–271.
14. Prather MJ. Time scales in atmospheric chemistry: coupled perturbations to N_2O, NO_y, and O_3. *Science*. 1998;279(5355):1339–1341.
15. Gligorovski S, Strekowski R, Barbati S, Vione D. Environmental implications of hydroxyl radicals (OH). *Chem Rev*. 2015;115(24):13051–13092.
16. Lin CL, DeMore WB. Reactions of Atomic Oxygen $O(^1D)$ with methane and ethane. *J Phys Chem*. 1973;77(7):863–869.
17. Luntz AC. Chemical dynamics of the reactions of $O(^1D_2)$ with saturated hydrocarbons. *J Chem Phys*. 1980;73(3):1143–1152.
18. Heidner III RF, Husain D. Electronically excited oxygen atoms, $O(^1D)$. A time-resolved study of the collisional quenching by the gases H_2, D_2, CH_4, NO, NO_2, N_2O, and C_3O_2 using atomic absorption spectroscopy in the vacuum ultraviolet. *Int J Chem Kinet*. 1973;5(5):819–831.
19. Yang X. Multiple channel dynamics in the $O(^1D)$ reaction with alkanes. *PCCP*. 2006;8(2):205–215.
20. Wada S-i, Obi K. Photochemical reaction dynamics of $O(^1D)$ with Saturated hydrocarbons, CH_4, C_2H_6, and C_3H_8, under bulk conditions and in van der Waals complexes. *J Phys Chem A*. 1998;102(20):3481–3491.
21. Osif Terr L, Simonaitis R, Heicklen J. The reactions of $O(^1D)$ and HO with CH_3OH. *J Photochem*. 1975;4(4):233–240.
22. Goldstein N, Wiesenfeld JR. Dynamics of $O(^1D_2)$ reactions with bifunctional substrates: alcohols and thiols. *J Chem Phys*. 1983;78(11):6725–6731.
23. Matsumi Y, Inagaki Y, Kawasaki M. Isotopic branching ratios and translational energy release of H and D atoms in the reaction of $O(^1D)$ with CH_3OD and CD_3OH. *J Phys Chem*. 1994;98(14):3777–3781.
24. Huang C-K, Xu Z-F, Nakajima M, et al. Dynamics of the reactions of $O(^1D)$ with CD_3OH and CH_3OD studied with time-resolved Fourier-transform IR spectroscopy. *J Chem Phys*. 2012;137(16):164307.
25. Hays BM, Widicus W, Susanna L. Theoretical examination of $O(^1D)$ insertion reactions to form methanediol, methoxymethanol, and aminomethanol. *J Phys Chem A*. 2013;117(32):7142–7148.
26. Zhong H, Yan C, Teng CC, et al. Kinetic studies of excited singlet oxygen atoms $O(^1D)$ reactions with fuels in plasma assisted combustion. In: AIAA Scitech 2019 Forum; 2019:2065.
27. Chen M-W, Rotavera B, Chao W, Zádor J, Taatjes CA. Direct measurement of OH and HO_2 formation in R + O_2 reactions of cyclohexane and tetrahydropyran. *PCCP*. 2018;20(16):10815–10825.
28. DeSain JD, Ho AD, Taatjes CA. High-resolution diode laser absorption spectroscopy of the O–H stretch overtone band (2, 0, 0)←(0, 0, 0) of the HO_2 radical. *J Mol Spectrosc*. 2003;219(1):163–169.
29. Wallington TJ, Dagaut P, Kurylo MJ. UV Absorption cross sections and reaction kinetics and mechanisms for peroxy radicals in the gas phase. *Chem Rev*. 1992;92(4):667–710.

30. Heard DE, Pilling MJ. Measurement of OH and HO_2 in the troposphere. *Chem Rev*. 2003;103(12):5163–5198.
31. Assali M, Rakovsky J, Votava O, Fittschen Christa. Experimental determination of the rate constants of the reactions of HO_2 + DO_2 and DO_2 + DO_2. *Int J Chem Kinet*. 2020;52(3):197–206.
32. Thiebaud J, Fittschen C. Near infrared Cw-CRDS coupled to laser photolysis: spectroscopy and kinetics of the HO_2 radical. *Appl Phys B*. 2006;85(2-3):383–389.
33. Ren W, Davidson DF, Hanson RK. IR Laser absorption diagnostic for C_2H_4 in shock tube kinetics studies. *Int J Chem Kinet*. 2012;44(6):423–432.
34. Nizkorodov SA, Harper WW, Blackmon BW, Nesbitt DJ. Temperature dependent kinetics of the OH/HO_2/O_3 Chain Reaction by Time-resolved IR Laser Absorption Spectroscopy. *J Phys Chem A*. 2000;104(17):3964–3973.
35. Yan C, Kocevska S, Krasnoperov LN. Kinetics of the reaction of CH_3O_2 radicals with OH studied over the 292–526 K temperature range. *J Phys Chem A*. 2016;120(31):6111–6121.
36. Brumfield B, Sun W, Ju Y, Wysocki G. Direct in situ quantification of HO_2 from a flow reactor. *J Phys Chem Lett*. 2013;4(6):872–876.
37. Teng CC, Yan C, Rousso A, Chen T, Ju Y, Wysocki G. HO_2 Detection in a photolysis reactor using Faraday rotation spectroscopy. In: Conference on Lasers and Electro-Optics: Applications and Technology; 2018: ATh3P–1.
38. Teng CC, Yan C, Zhong H, et al. HO_2 radical measurements in a photolysis reactor using line-locked Faraday rotation spectroscopy. In: Optics and Photonics for Energy and the Environment; 2018: EW3A–6.
39. Zhong H, Yan C, Teng CC, Ma G, Wysocki G, Ju Y. Kinetic study of reaction C_2H_5 + HO_2 in a photolysis reactor with time-resolved Faraday rotation spectroscopy. *Proc Combust Inst*; 2020.
40. Yan C, Teng CC, Chen T, et al. The kinetic study of excited singlet oxygen atom O(^{1}D) reactions with acetylene. *Combust Flame*. 2020;212:135–141.
41. Kato A, Cvetanović R. Reaction of oxygen atoms with ethanol. *Can J Chem*. 1967;45(16):1845–1861.
42. Wu C-W, Lee Y-P, Xu S, Lin M-C. Experimental and theoretical studies of rate coefficients for the reaction O(^{3}P) + C_2H_5OH at high temperatures. *J Phys Chem A*. 2007;111(29):6693–6703.
43. Sander S, Golden D, Kurylo M, et al., *Chemical Kinetics and Photochemical Data for Use in Atmospheric Studies: Evaluation Number 15*. JPL Publication 06-2. Pasadena, CA: Jet Propulsion Laboratory, California Institute of Technology; 2006.
44. Baklanov AV, Krasnoperov LN. Oxalyl chloride a clean source of chlorine atoms for kinetic studies. *J Phys Chem A*. 2001;105(1):97–103.
45. MicroMath. *Scientist*. Version 2.0; 1995.
46. Sarathy SM, Oßwald P, Hansen N, Kohse-Höinghaus K. Alcohol combustion chemistry. *Prog Energy Combust Sci*. 2014;44:40–102.
47. Zádor J, Taatjes CA, Fernandes RX. Kinetics of elementary reactions in low-temperature autoignition chemistry. *Prog Energy Combust Sci*. 2011;37(4):371–421.
48. Anglada JM, Olivella S, Solé A. Mechanistic study of the CH_3O_2 + HO_2→ CH_3O_2H + O_2 reaction in the gas phase. Computational evidence for the formation of a hydrogen-bonded diradical complex. *J Phys Chem A*. 2006;110(18):6073–6082.
49. Hasson AS, Tyndall GS, Orlando JJ. A product yield study of the reaction of HO_2 radicals with ethyl peroxy ($C_2H_5O_2$), acetyl peroxy ($CH_3C(O)O_2$), and acetonyl peroxy ($CH_3C(O)CH_2O_2$) radicals. *J Phys Chem A*. 2004;108(28):5979–5989.
50. Zádor J, Fernandes RX, Georgievskii Y, Meloni G, Taatjes CA, Miller JA. The reaction of hydroxyethyl radicals with O_2: a theoretical analysis and experimental product study. *Proc Combust Inst*. 2009;32(1):271–277.
51. Sander S, Friedl R, Abbatt J, et al., *Chemical Kinetics and Photochemical Data for Use in Atmospheric Studies: Evaluation Number 17*.. JPL Publication 10-6. Pasadena, CA: Jet Propulsion Laboratory, California Institute of Technology; 2011.
52. Dunlea EJ, Talukdar RK, Ravishankara AR. Kinetic studies of the reactions of O_2 ($b\Sigma_g$) with several atmospheric molecules. *J Phys Chem A*. 2005;109(17):3912–3920.
53. Bedjanian Y, Le Bras G, Poulet G. Kinetic study of OH + OH and OD + OD reactions. *J Phys Chem A*. 1999;103(35):7017–7025.
54. Sangwan M, Chesnokov EN, Krasnoperov Lev N. Reaction OH + OH studied over the 298–834 K temperature and 1–100 bar pressure ranges. *J Phys Chem A*. 2012;116(24):6282–6294.
55. Carr SA, Blitz MA, Seakins PW. Site-specific rate coefficients for reaction of OH with ethanol from 298 to 900 K. *J Phys Chem A*. 2011;115(15):3335–3345.
56. Atkinson R, Baulch DL, Cox RA, et al. Evaluated kinetic and photochemical data for atmospheric chemistry: volume i – gas phase reactions of O_x, HO_x, NO_x and SO_x species. *Atmos Chem Phys*. 2004;4(6):1461–1738.
57. Tsang W, Hampson RF. Chemical kinetic data base for combustion chemistry. Part I. Methane and related compounds. *J Phys Chem Ref Data*. 1986;15(3):1087–1279.
58. Zellner R, Erler K, Field D. Kinetics of the recombination reaction OH + H + M ⟶ H_2O + M at low temperatures. *Symp (Int) Combust*. 1977;16:939–948.
59. Jiménez E, Gierczak T, Stark H, Burkholder JB, Ravishankara A. Reaction of OH with HO_2NO_2 (peroxynitric acid): rate coefficients between 218 and 335 K and product yields at 298 K. *J Phys Chem A*. 2004;108(7):1139–1149.
60. Keyser LF. Kinetics of the Reaction OH + HO_2⟶ H_2O + O_2 from 254 to 382 K. *J Phys Chem*. 1988;92(5):1193–1200.
61. Baulch D, Cobos C, Cox R, et al. Evaluated kinetic data for combustion modelling. *J Phys Chem Ref Data*. 1992;21(3):411–734.
62. Mousavipour SH, Saheb V. Theoretical study on the kinetic and mechanism of H + HO_2 reaction. *Bull Chem Soc Jpn*. 2007;80(10):1901–1913.
63. Hippler H, Rahn R, Troe J. Temperature and pressure dependence of ozone formation rates in the range 1–1000 bar and 90–370 K. *J Chem Phys*. 1990;93(9):6560–6569.
64. Troe J, Warnatz J. Evaluated kinetic data for combustion modelling supplement I. *J Phys Chem Ref Data*. 1994;23:847.
65. Atkinson R, Baulch DL, Cox RA, et al. Evaluated kinetic, photochemical and heterogeneous data for atmospheric chemistry: supplement V. IUPAC Subcommittee on Gas Kinetic Data Evaluation for Atmospheric Chemistry. *J Phys Chem Ref Data*. 1997;26(3):521–1011.
66. Atkinson R, Baulch DL, Cox RA, et al. Summary of evaluated kinetic and photochemical data for atmospheric chemistry. IUPAC Subcommittee on Gas Kinetic Data Evaluation for Atmospheric Chemistry. 2001:20.

67. Atkinson R, Baulch DL, Cox RA, Hampson RF Jr, Kerr JA, Troe J. Evaluated kinetic and photochemical data for atmospheric chemistry: supplement III. IUPAC Subcommittee on Gas Kinetic Data Evaluation for Atmospheric Chemistry. *J Phys Chem Ref Data*. 1989;18(2):881–1097.
68. Batt L, Burrows JP, Robinson GN. On the isomerisation of the methoxy radical relevance to atmospheric chemistry and combustion. *Chem Phys Lett*. 1981;78(3):467–470.
69. Tsang W. Chemical kinetic data base for combustion chemistry. Part 2. Methanol. *J Phys Chem Ref Data*. 1987;16(3):471–508.
70. Hassinen E, Koskikallio J. Flash Photolysis of methyl acetate in gas phase. products and rate constants of reactions between methyl, methoxy and acetyl radicals. *Acta Chem Scand, Ser A*. 1979;33(8):625–630.
71. Reinhard Z. Recent advances in free radical kinetics of oxygenated hydrocarbon radicals. *J Chim Phys*. 1987;84:403–407.
72. Hoyermann K, Loftfield NS, Sievert R, Wagner HG. Mechanisms and rates of the reactions of CH_3O and CH_2OH radicals with H atoms. *Symp (Int) Combust*. 1981;18:831–842.
73. Grotheer HH, Nesbitt FL, Klemm RB. Absolute rate constant for the reaction of oxygen O(^{3}P) with ethanol. *J Phys Chem*. 1986;90(11):2512–2518.
74. Grotheer H-H, Rieketr G, Walter D, Just T. Reactions of hydroxymethyl and hydroxyethyl radicals with molecular and atomic oxygen. *Symp (Int) Combust*. 1989;22:963–972.
75. Herron JT, Huie RE. Rate constants for the reactions of atomic oxygen O(^{3}P) with organic compounds in the gas phase. *J Phys Chem Ref Data*. 1973;2(3):467–518.
76. Bartels M, Hoyermann K, Sievert R. Elementary reactions in the oxidation of ethylene: the reaction of OH radicals with ethylene and the reaction of C_2H_4OH radicals with H atoms. *Symp (Int) Combust*. 1982;19:61–72.
77. Anastasi C, Simpson V, Munk J, Pagsberg P. UV spectrum and the kinetics and reaction pathways of the self-reaction of hydroxyethyl radicals. *J Phys Chem*. 1990;94(16):6327–6331.
78. Xu ZF, Xu K, Lin M-C. Thermal decomposition of ethanol. 4. Ab initio chemical kinetics for reactions of H atoms with CH_3CH_2O and CH_3CHOH radicals. *J Phys Chem A*. 2011;115(15):3509–3522.
79. Noell AC, Alconcel LS, Robichaud DJ, Okumura M, Sander SP. Near-infrared kinetic spectroscopy of the HO_2 and $C_2H_5O_2$ self-reactions and cross reactions. *J Phys Chem A*. 2010;114(26):6983–6995.

SUPPORTING INFORMATION

Additional supporting information may be found online in the Supporting Information section at the end of the article.

How to cite this article: Zhong H, Yan C, Teng CC, Chen TY, Wysocki G, Ju Y. Kinetic studies of excited singlet oxygen atom O(^{1}D) reactions with ethanol. *Int J Chem Kinet*. 2021;1–14. https://doi.org/10.1002/kin.21474